Sustainable
Energy & Fuels

PAPER

View Article Online
View Journal | View Issue

Cite this: *Sustainable Energy Fuels*, 2026, **10**, 364

Tailoring supercapacitor performance *via* sulfur engineering in ternary CoNiMoS electrodes

Trupti Tanaya Mishra,[a] Manisha Sadangi,[bc] J. N. Behera, *[bc] Mohua Chakraborty*[a] and Dhrubojyoti Roy*[a]

In this work, porous CoNiMoS (CNMS)-based ternary nanoflower arrays were successfully grown on nickel foam (NF) using a two-step strategy involving hydrothermal synthesis followed by a solvothermal sulfidation process. The influence of sulfidation concentration was systematically investigated to optimize the electrochemical performance. The optimized CNMS@NF electrode exhibits a pronounced charge–discharge activation behaviour and delivers a high specific capacitance of 1940 F g^{-1} at 1 A g^{-1}. The hierarchical porous architecture, derived from hydroxide precursors, enables improved electrolyte diffusion and efficient exposure of active sites. Notably, this structural evolution leads to a substantial reduction in solution impedance from 4.1 Ω to 2.12 Ω, enhancing charge transport kinetics. The electrode achieves an impressive energy density of 349.2 Wh kg^{-1} and a power density of 1631 W kg^{-1}, while retaining 70% of its initial capacitance after 4000 charge–discharge cycles, demonstrating excellent long-term stability. The superior electrochemical performance is attributed to the synergistic interaction among Co, Ni, and Mo species and the enrichment of S^{2-} anions, which collectively stabilize the nanoflower structure and promote robust redox activity. These findings position the CNMS@NF electrode as a promising candidate for high-performance energy storage applications.

Received 8th August 2025
Accepted 26th November 2025

DOI: 10.1039/d5se01081k

rsc.li/sustainable-energy

Introduction

The growing concerns over fossil fuel depletion and climate change have intensified the global pursuit of sustainable and clean energy solutions. In this context, the development of high-performance energy storage technologies has become a central focus of modern research.[1] Among the various energy storage systems, supercapacitors also known as ultracapacitors-have gained significant attention due to their unique advantages over conventional batteries, including ultrafast charge–discharge rates, high power density, long cycle life, and wide operational temperature ranges.[2–5] These features make supercapacitors ideal for a range of applications, such as portable electronics, telecommunications, hybrid vehicles, and next-generation wearable technologies.[6–8] Despite these advantages, the relatively low energy density of supercapacitors compared to traditional batteries continues to limit their broader deployment.[9] Therefore, current research is directed toward improving energy density while preserving their inherent strengths.[10] One approach involves designing advanced electrode materials with enhanced electrochemical activity. Conductive substrates like nickel foam,[11] carbon cloth,[12] and graphene foam[13] have been widely explored to directly grow active materials, offering increased electrical conductivity, structural support, and binder-free configurations.[14] Another strategy incorporates redox-active transition metals such as iron (Fe),[15,16] manganese (Mn),[17] and molybdenum (Mo)[18–20] to increase the density of electrochemically active sites, thereby enhancing charge storage capacity.

Among various material classes, transition metal compounds—particularly hydroxides (TMHs), oxides (TMOs), tellurides and sulfides (TMSs)—have shown immense promise due to their high theoretical capacitance and rich electrochemical behavior.[21–24] However, TMHs and TMOs often suffer from low electrical conductivity and limited active surface areas due to their wide bandgaps and aggregation tendency.[25–27] In contrast, TMSs exhibit narrower bandgaps, better conductivity, and rich redox chemistry arising from their multiple oxidation states and versatile crystal structures, making them superior candidates for supercapacitor electrodes.[28,29] Recent studies indicate that multi-metallic sulfides outperform their single-metal analogues in electrochemical performance due to synergistic effects and improved structural stability.[30–32] For example, Yang *et al.* (2021) fabricated a flexible $NiCo_2O_4$@$NiCoMnS_4$ electrode, achieving a remarkable specific capacity of 4836.2 mF cm^{-2}, significantly outperforming the individual components.[33] Similarly, Sun *et al.* (2023) reported a 3D NiCoMoS@$Mo_{0.75}$-LDH electrode with a specific capacitance of 1158 C g^{-1} and

---

[a] Department of Physics, C. V. Raman Global University, Bhubaneswar, Odisha-752054, India. E-mail: dhrubojyoti.roy@cgu-odisha.ac.in

[b] School of Chemical Sciences, National Institute of Science Education and Research (NISER), An OCC of Homi Bhabha National Institute (HBNI), Khurda, Odisha752050, India. E-mail: jnbehera@niser.ac.in

[c] Centre for Interdisciplinary Sciences (CIS), NISER, Jatni, 752050, Odisha, India

excellent cyclic stability.[34] Iqbal *et al.* (2023) demonstrated enhanced performance in a $Co_{0.5}Mn_{0.5}S$-based hybrid electrode with a specific capacity of 542.8 C g^{-1} at 2 A g^{-1}, highlighting the benefit of multi-metal synergy.[35] Chavan *et al.* (2023) synthesized a MnCoNiS nanostructure on nickel foam, achieving 2831.85 F g^{-1} and excellent durability after 10 000 cycles, attributed to optimized material design and multi-element interactions.[36]

Herein, we report a novel *in situ* synthesis approach to engineer binder-free ternary sulfide electrodes by incorporating sulfur (S^{2-}) into a CoNiMo-based hydroxide framework. A cost-effective two-step hydrothermal and solvothermal route was employed to grow porous flower-like CoNiMoS (CNMS) nanostructures directly on nickel foam (NF), denoted as CNMS@NF. The NF substrate provides high conductivity, mechanical stability, and a 3D porous network, which facilitates uniform material growth, minimizes agglomeration, and enhances electron and ion transport. The precursor CoNiMo hydroxide (CNMH) was synthesized at 150 °C for 6 hours, and subsequent sulfidation at 120 °C for 3 hours produced the optimized CNMS sample (termed CNMS3). The CNMS3 electrode demonstrated significantly improved performance over its hydroxide counterpart, attributed to its unique flower-like morphology and synergistic multi-metallic interactions. The optimized electrode delivered an excellent specific capacitance of ~1940 F g^{-1} at 1 A g^{-1} and retained 70% of its capacitance after 4000 cycles at 100 mV s^{-1}, confirming its potential for high-performance supercapacitor applications.

Experimental section

Materials

Polyvinylidine fluoride (PVDF) (>99.9% purity), sodium molybdate dihydrate ($Na_2MoO_4.2H_2O$) (>99.9% purity), urea ($CO(NH_2)_2$) (>99.9% purity), sodium sulfide (Na_2S) (>99.9% purity), nickel nitrate hexahydrate ($Ni(NO_3)_2\cdot 6H_2O$) (>99.9% purity), and Cobalt nitrate hexahydrate ($Co(NO_3)_2\cdot 6H_2O$) (>99.9% purity) were all acquired from Sigma Aldrich. Ammonium fluoride (96.0%, NH_4F, Alfa Aesar), carbon black acquired from MTI Corp. The supplier of ethanol was Merck. Nickel foam was used from Vritra technologies (>99% purity).

Nickel foam cleaning

The NF was pre-treated in concentrated HCl to remove surface oxide films. Initially, several pieces of NF (0.5 × 1 cm^2) were cut and ultrasonicated in acid for 10 minutes. Further it was cleaned in deionized water and ethanol for removal of impurities. The weight of each nickel foam was checked three times to ensure accuracy and minimize errors.

In situ growth of CoNiMo hydroxide (CNMH) electrode: step-1

A precursor solution was prepared by dissolving 5 mmol of $Co(NO_3)_2\cdot 6H_2O$, 1.25 mmol of $Ni(NO_3)_2\cdot 6H_2O$, 6.25 mmol of $Na_2MoO_4\cdot 2H_2O$, 75 mmol urea, and 37.5 mmol of NH_4F in 35 ml deionized water. The mixture was stirred for 30 minutes to form a homogeneous, transparent, pink solution. Next, the solution was placed in a 50 ml Teflon-lined stainless-steel autoclave and heated at 150 °C for 6 hours. After cooling, the product was washed with deionized water and ethanol to remove impurities, and then dried at 60 °C for 12 hours. The final product, denoted as CNMH@NF, had an average mass loading of 0.5 mg cm^{-2}. The CNMH@NF were also tried at various temperature and duration conditions (as shown in Fig. S1) among which the performance of the electrode grown at 150 °C for 6 hours was observed to be ideal for supercapacitor application.

Preparation of CoNiMoS (CNMS) modified electrodes: step-2

The CNMH@NF was submerged vertically in an aqueous solution containing varying concentrations ($X = 1.0, 0.5, 0.25, 0.125$ mmol) of $Na_2S\cdot 9H_2O$ for sulfurization. The prepared solution was a mixture of distilled water and ethanol in a ratio of 2 : 3, resulting in a total volume of 35 ml.[37] The solution was then transferred to a 50 ml autoclave and heated in an oven at 120 °C for 3 hours. After cooling, the tri-metal sulfide-coated NF was washed with absolute ethanol and distilled water, and dried in a vacuum drying oven at 60 °C for 4 hours. This process yielded CoNiMoS nanoflowers. The resulting samples were labelled as CNMS1, CNMS2, CNMS3, and CNMS4 from higher to lower concentration of $Na_2S\cdot 9H_2O$, respectively. After the sulfurization process, the mass loading of the material remained at 0.5 mg cm^{-2}. Several other temperatures were also tried for synthesis which is given in the SI. The fabrication process of the electrodes is diagrammatically represented in Scheme 1.

Characterization techniques

The crystal structure of the powder samples was analyzed using X-ray diffraction (XRD) on a Bruker D8 Advance diffractometer system with Cu Kα radiation ($\lambda = 1.5418$ Å). Raman spectroscopy was conducted using a LabRAM HR Raman Spectrometer (Horiba) with a 532 nm laser. The surface morphology was examined using field emission scanning electron microscopy (FESEM) on a Zeiss instrument Pvt. Ltd, Germany. To avoid the effect of NF, the sample was ultrasonicated for 30 min to obtain the diluted sample for performing transmission electron

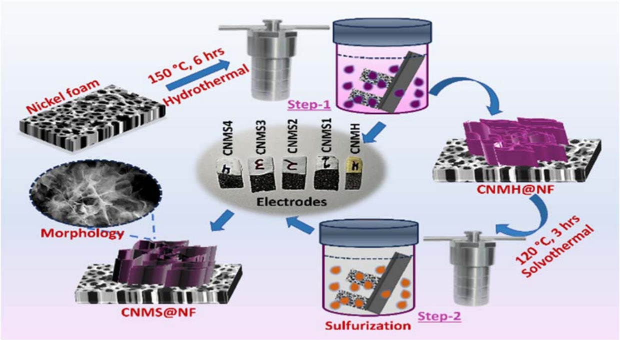

Scheme 1 Schematic stepwise representation of *in situ* growth of CoNiMo hydroxide (CNMH) electrode using hydrothermal process and then preparation of CoNiMoS (CNMS) modified electrode *via* sulfurization technique using solvothermal process.

microscopy (TEM). TEM analysis of the samples was observed on a JEOL 2100F instrument equipped with high-resolution TEM (HRTEM) at 200 kV. Brunauer–Emmett–Teller (BET) desorption/adsorption analysis was performed on a Quanta Chrome Instruments system at 77 K to assess the specific surface area and porosity. The degassing of the sample prior to BET measurement was carried out at 80 °C for 12 hours to ensure complete removal of adsorbed moisture and gases. X-ray photoelectron spectroscopy (XPS) was conducted on an Omicron Multiprobe system, featuring a monochromatized Al Kα source (1486.6 eV) and EA125 hemispherical electron analyzer, to investigate the surface composition and chemical state. Data analysis was performed using PeakFit41 software, incorporating Shirley method with background correction and Gaussian–Lorentzian curve fitting. The elemental composition of the synthesized electrode was determined using inductively coupled plasma-optical emission spectroscopy (ICP-OES) on an iCAP 7000 instrument.

Electrochemical characterizations

The electrochemical performance such as cyclic voltammetry (CV), galvanostatic charge–discharge (GCD) and electrochemical impedance spectroscopy (EIS) of the synthesized materials was assessed using a three-electrode cell configuration on a Biologic SP-200 workstation. The cell was assembled with the synthesized materials as the working electrode, a platinum electrode as counter one and an Hg/HgO reference electrode dipped in 3 M KOH solution as the electrolyte. A 3 M KOH solution was used as the electrolyte since it provides high ionic conductivity and stability, enabling efficient ion transport and reliable evaluation of the electrode's electrochemical performance. This concentration offers a good balance, avoiding corrosion at higher concentrations and poor utilization at lower ones (Fig. S2).[38] CV measurements were conducted within a potential window of 0-0.6 V at various scan rates. The potential window of 0–0.6 V was selected to ensure complete utilization of the reversible redox reactions of Co, Ni, and Mo sulfides while maintaining electrolyte stability. Extending the range beyond 0.6 V caused CV distortion and oxygen evolution (Fig. S3). To activate the electrode, 150 CV cycles at 50 mV s^{-1} were performed. GCD curves were obtained at different current densities between 0–0.4 V. EIS measurements were also carried out by applying an alternating voltage with a 5 mV amplitude at the open circuit potential, over a frequency range of 10 mHz to 200 kHz. The specific capacitance (C_s) (F g^{-1}) and specific capacity (C_{sp}) (mAh g^{-1}) of the electrode can be calculated from both CV and GCD using the following equations respectively.[39]

$$C_s(\mathrm{CV}) = \frac{\int IV\mathrm{d}V}{2ms\Delta V} \tag{1}$$

$$C_s(\mathrm{GCD}) = \frac{I}{m} \times \frac{\Delta t}{\Delta v} \tag{2}$$

$$C_{sp}(\mathrm{CV}) = \frac{\int IV\mathrm{d}V}{2ms} \tag{3}$$

$$C_{sp}(\mathrm{GCD}) = \frac{I\Delta t}{m} \tag{4}$$

where, I and V are current and potential in CV test, m is the active mass loading, s is the scan rate, Δv and Δt are potential window and discharging time in GCD respectively.

The energy density (E, Wh kg^{-1}) and power density (P, W kg^{-1}) of the electrode material were calculated using eqn (5) and (6), respectively.

$$E = \frac{1}{2}C_s(\Delta v)^2 \tag{5}$$

$$P = 3600 \times \frac{E}{t} \tag{6}$$

Results and discussions

The structural features of the synthesized materials were first investigated using X-ray diffraction (XRD). As shown in Fig. 1(a), the XRD pattern of the CoNiMo-hydroxide powder displays prominent peaks corresponding to $Ni(CO_3)(OH)_2 \cdot 4H_2O$ (PDF No: 35-0501) and $Co(CO_3)_{0.5}(OH) \cdot 0.11H_2O$ (PDF No: 48-0083). Notably, only two distinct diffraction peaks are observed, corresponding to the (221) and (412) planes of the $CoNi(CO_3)(OH) \cdot 0.11H_2O$ phase, confirming the successful formation of the LDH structure.[37,40] The XRD pattern of CNMS3 (Fig. 1(b)) reveals the emergence of new diffraction peaks near 27°, attributed to the (311) plane of Co_3S_4 (PDF No: 47-1738), along with additional low-intensity peaks in the 60°–75° range that correspond to NiS (PDF No: 02-1280). These peaks, along with residual signals from $Ni(CO_3)(OH)_2 \cdot 4H_2O$ and $Co(CO_3)_{0.5}(OH) \cdot 0.11H_2O$, indicate the coexistence of sulfide and carbonate hydroxide phases. The presence of Co_3S_4 and NiS phases is consistent across all CNMS samples, as illustrated in Fig. 1(c). To further examine surface functionalities, Raman spectroscopy was performed. As shown in Fig. 1(d), the CNMS electrodes exhibit two characteristic vibrational peaks. The first peak at 337 cm^{-1} is attributed to the Co–O–Mo bond vibration, while the more intense peak at 935 cm^{-1} corresponds to the Mo–O stretching mode. The presence of the Mo–O vibration suggests successful intercalation of MoO_4^{2-}, while the Co–O–Mo vibration confirms covalent bonding between the metal centres.[41,42] Post-sulfurization, no new Raman peaks were observed; however, a slight red shift in the 935 cm^{-1} peak was detected with increasing sulfur content, which may arise from changes in bond length or intermolecular interactions.[43] The chemical composition and oxidation states of the elements were analyzed *via* X-ray photoelectron spectroscopy (XPS). The wide-scan survey spectra (Fig. S4) confirm the presence of Ni, Co, and Mo in CNMH, and additional sulfur peaks in CNMS3, validating successful sulfur incorporation. The high-resolution Ni 2p spectrum of CNMH (Fig. 2(a)) reveals six peaks: two corresponding to Ni^{2+} at 855.8 and 873.3 eV, two for Ni^{3+}at 860.0 and 877.5 eV, and two satellite peaks at 861.8 and 880.8 eV. In CNMS3, the Ni^{2+} $2p_{3/2}$ and $2p_{1/2}$ peaks exhibit negative shifts of 0.8 eV and 0.5 eV, respectively, while Ni^{3+} $2p_{3/2}$ shifts by 0.3 eV. The Ni^{2+} satellite peak in CNMS3 appears at

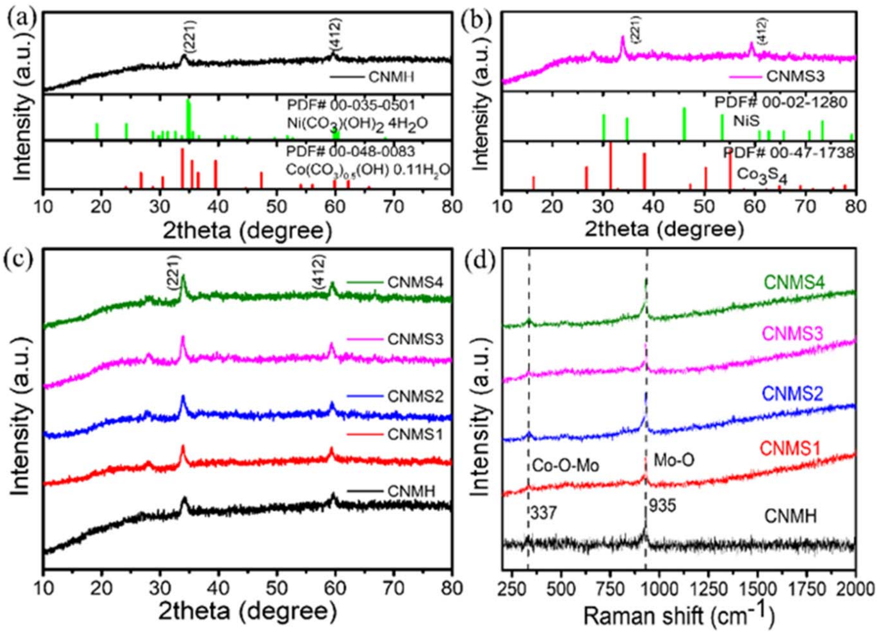

Fig. 1 XRD plot of (a) CNMH sample, (b) CNMS3 sample, (c) combined XRD plot of all electrodes, (d) Raman plot of all the electrodes.

863.1 eV, suggesting enhanced electronic interactions and chemical bonding within the CNMH/CNMS heterostructure.[35,37,38] Similarly, the Co 2p spectrum (Fig. 2(b)) of CNMH shows two spin–orbit doublets: peaks at 780.5 and 796.6 eV are assigned to Co^{2+}, while those at 779.5 and 795.2 eV correspond to Co^{3+}. Satellite peaks are observed at 785.1 and 802.4 eV.[39,40] In CNMS3, the Co^{2+} $2p_{3/2}$ and $2p_{1/2}$ peaks shift negatively by 0.3 eV and 0.4 eV, respectively, with satellite peaks observed at 784.8 and 802.2 eV. These shifts indicate strong synergistic electronic interactions in the CNMS3 nanoarchitecture.[41,42] The Mo 3d spectra (Fig. 2(c)) for CNMH show two distinct peaks at 231.5 and 234.6 eV, corresponding to Mo^{6+} $3d_{5/2}$ and $3d_{3/2}$, respectively, confirming the presence of Mo^{6+} species.[44] In CNMS3, these peaks shift positively by 0.6 eV. Additionally, a new peak appears at 234.7 eV, indicative of Mo^{5+} species, confirming partial reduction during sulfurization.[45] The O 1s spectrum (Fig. 2(d)) shows a dominant peak at 529.7 eV, attributed to metal–oxygen bonds. Deconvolution reveals additional components at 531.2 and 532.7 eV, assigned to adsorbed water and metal–hydroxide species, respectively, consistent with literature values.[46] Lastly, the S 2p spectrum of CNMS3 (Fig. 2(e)) exhibits two main peaks at 161.6 and 162.7 eV, corresponding to metal–sulfur (S^{2-}) bonds such as Co–S, Ni–S, and Mo–S. A third peak at 168.8 eV is assigned to

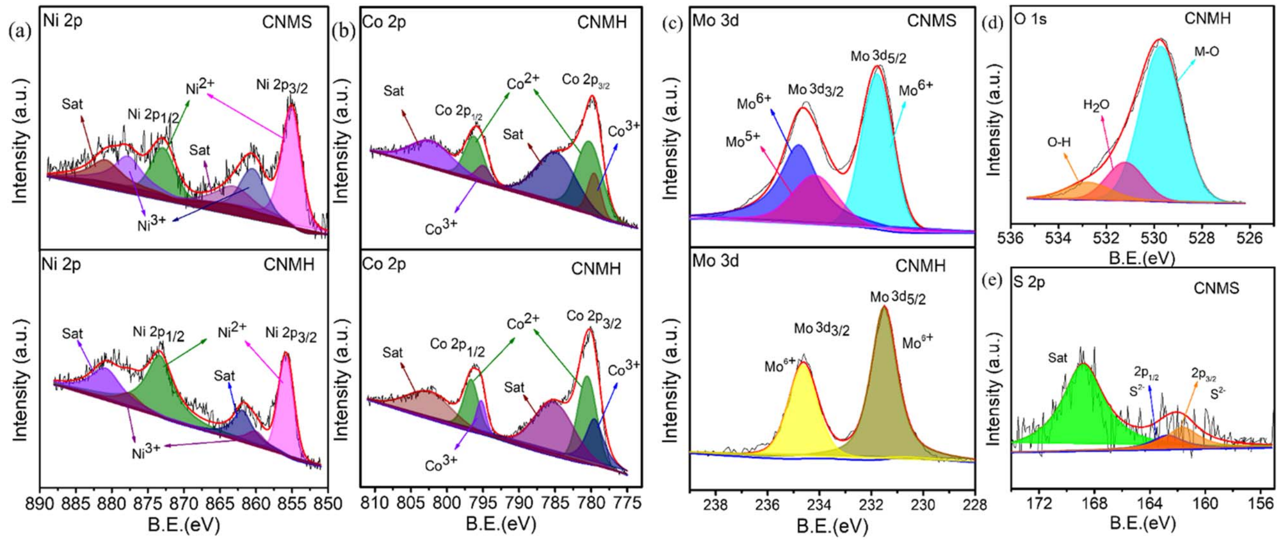

Fig. 2 Deconvoluted XPS spectra of CNMS3 and CNMH (a) Ni 2p, (b) Co 2p, (c) Mo 3d, (d) O 1s of CNMH (e) S 2p of CNMS3.

a shake-up satellite, further confirming the successful formation of metal sulfide phases.[47] The evolution of surface morphology from CNMH to various CNMS samples at different sulfurization concentrations is captured in the SEM images (Fig. 3(a–e)). As shown in Fig. 3(a), CNMH features well-defined flower-like nanostructures. Upon sulfurization with a high sulfur concentration (1 mmol; Fig. 3(b)), the nanoflowers retain their general architecture but begin to exhibit fragmentation. Conversely, at lower sulfur concentrations (0.5, 0.25 and 0.125 mmol; Fig. 3(c–e)), the nanoflower morphology gradually collapses and aggregates, with structural deterioration becoming more pronounced at the lowest concentration (0.125 mmol). Among these, the CNMS sample prepared with 0.25 mmol sulfur concentration (Fig. 3(d)) is identified as optimal, striking a favourable balance between porosity and structural integrity-an essential factor for maximizing active surface area. Interestingly, the morphology of the CNMS samples closely resembles the delicate, layered structure of a desert "sand rose," as illustrated in Fig. 3(f). This visual analogy highlights the intricacy of the nanoflower architecture. The optimization of sulfur concentration is critical; excessive sulfur can induce structural instability and defect formation, while insufficient sulfur results in incomplete conversion and suboptimal performance. The CNMS3 sample emerges as the best-performing candidate, exhibiting an optimal degree of sulfurization with a preserved porous network, essential for high-performance electrochemical applications.

To gain deeper insights into the microstructure of CNMH and CNMS3, Transmission Electron Microscopy (TEM) characterization was conducted. TEM analysis reveals ultrathin, interconnected nanosheets forming the nanoflower structure, consistent with the SEM observations. The Selected Area Electron Diffraction (SAED) patterns confirm the polycrystalline nature of both samples. For CNMS3 (Fig. 3(i), two distinct diffraction rings are observed, corresponding to the (222) planes of Co_3S_4 and the (103) planes of NiS. In contrast, CNMH (see Fig. S5 displays rings attributed to the (221) and (231) planes of $Co(CO_3)_{0.5}OH)\cdot 0.11H_2O$, and the (002) planes of $Ni(CO_3)(OH)_2\cdot 4H_2O$, aligning well with the XRD results and confirming the phase transformation upon sulfurization. Elemental composition and spatial distribution were further examined *via* Energy Dispersive X-ray Spectroscopy (EDS) mapping. The EDS results (Fig. S6 and S4) confirm the uniform dispersion of Co, Ni, and Mo in both CNMH and CNMS3 samples. The EDS spectrum of CNMS3 (Fig. 4) also reveals a marked decrease in oxygen content and the appearance of sulfur peaks, indicative of a successful conversion from hydroxide to sulfide. Additionally, sulfur-rich domains are evident in CNMS3, which could enhance charge transfer kinetics and contribute to superior electrochemical behaviour. Nitrogen adsorption–desorption isotherms were used to evaluate the surface area and pore characteristics of the samples. As presented in Fig. 5(a), both CNMH and CNMS3 display type IV isotherms with H_3 hysteresis loops, characteristic of

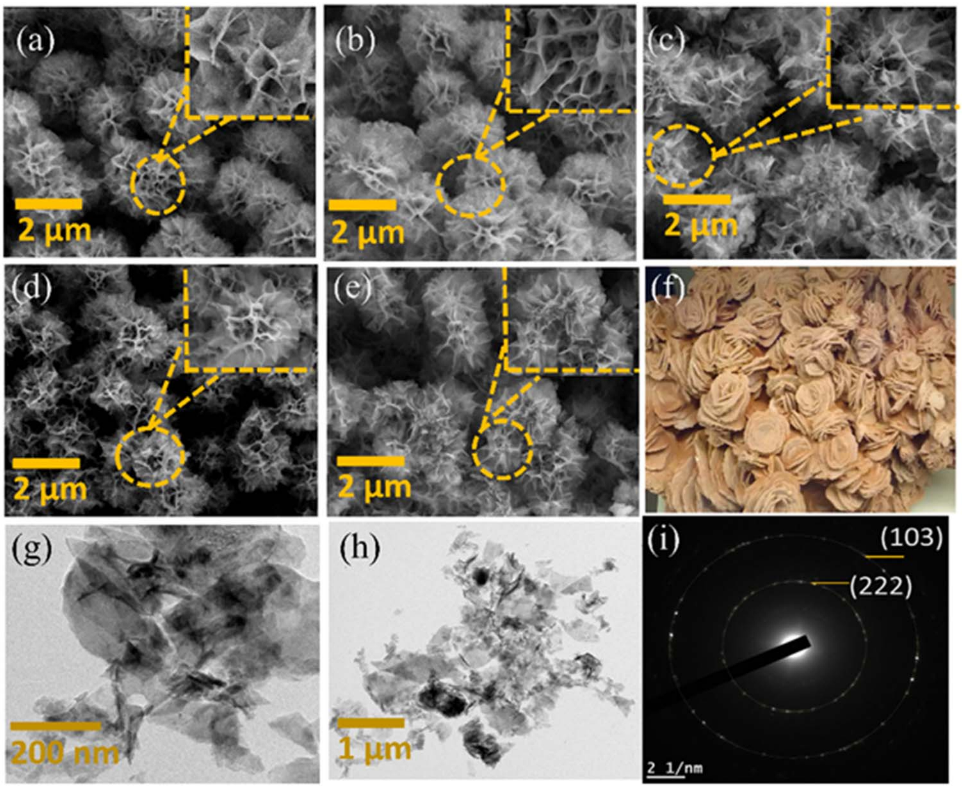

Fig. 3 SEM images of (a) CNMH@NF, (b) CNMS1@NF, (c) CNMS2@NF, (d) CNMS3@NF, (e) CNMS4@NF samples, (f) sand rose image, (g and h) TEM images of CNMS3@NF at different resolutions, (i) SAED pattern of CNMS3@NF.

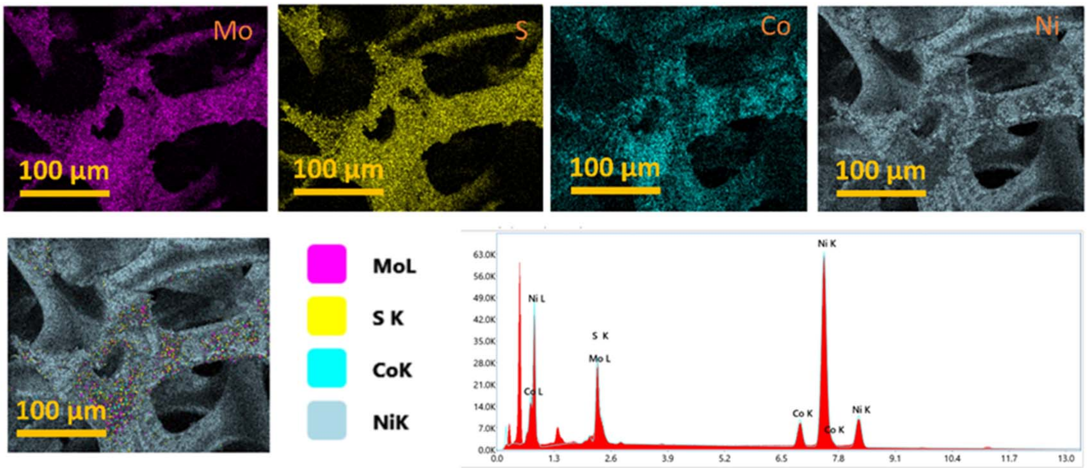

Fig. 4 EDS mapping images of Mo, S, Co, Ni elements in CNMS3@NF sample.

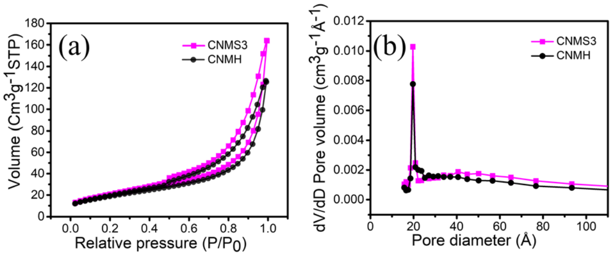

Fig. 5 (a) N_2 adsorption–desorption, (b) pore size distribution of CNMH and CNMS3 samples.

mesoporous materials.[48,49] Notably, CNMS3 exhibits a higher Brunauer–Emmett–Teller (BET) surface area of 72.48 $m^2\ g^{-1}$, compared to 66.7 $m^2\ g^{-1}$ for CNMH. This increase is attributed to the successful incorporation of sulfur into the hierarchical nanoflower structure, resulting in a more open framework and improved exposure of active sites. Fig. 5(b) further illustrates the pore size distribution, showing that both CNMH@NF and CNMS3@NF possess a mixed porosity profile comprising abundant mesopores and smaller micropores. The presence of mesopores in CNMS3, along with its higher specific surface area, is particularly advantageous for energy storage applications, as it provides enhanced ion diffusion pathways and better accessibility to electroactive sites.

This porous architecture not only supports efficient ion transport but also promotes improved electrode–electrolyte interaction, thereby boosting overall electrochemical capacitance.[50] The electrochemical properties of the synthesized samples were evaluated using a 3-electrode set up in 3 M KOH electrolyte. The CV behaviours of the samples were initially examined at a scan rate of 2 mV s^{-1}, with the results presented in Fig. 6(a). The CV curves of all samples exhibit prominent redox peaks, indicating a significant contribution of pseudocapacitive behaviour to their capacity. Notably, the CNMS3 composite displays a larger enclosed area in its CV curve compared to CNMH and other CNMS electrodes, suggesting that the sulfidation process enhances the electrochemical activity of the material. Fig. 6(b) represents the CV curves of the CNMS3 hybrid electrode at various scan rates (2–100 mV s^{-1}). With increasing scan rates, the redox peaks exhibit a noticeable shift towards the cathodic and anodic directions, respectively. Notably, the CV curves maintain their shape across different scan rates, indicating rapid ion diffusion and efficient electron transfer processes within the hybrid electrode.[51] The CV curves of all other electrodes with different scan rates are shown in Fig. S7. The specific capacitance of CNMS3 was further investigated at various scan rates in Fig. 6(c). Remarkably in Fig. 6(c), the material exhibited specific capacitance values of 2944.9 F g^{-1} (1767 mAh g^{-1}), 2315.1 F g^{-1} (1389 mAh g^{-1}), 1684.2 F g^{-1} (1010.5 mAh g^{-1}), 868.4 F g^{-1} (521 mAh g^{-1}), 444.2 F g^{-1} (266.5 mAh g^{-1}), and 211 F g^{-1} (126.6 mAh g^{-1}) at scan rates of 2, 5, 10, 25, 50, and 100 mV s^{-1}, respectively. This decrease in specific capacitance at higher scan rates can be attributed to the limited diffusion kinetics of electrolyte ions within the material. A consistent trend is observed across all samples, where the specific capacitance (specific capacity) varies similarly with the scan rate (Fig. S8). To quantify the kinetics of redox reactions at the electrode, the relationship between peak current (i) and scan rate (ν) was investigated using the following equation.[52]

$$i = a\nu^b \tag{7}$$

where a and b are adjustable coefficients. The value of b provides insight into the underlying kinetics, with $b = 1$ indicating a surface-controlled reaction characterized by pseudocapacitive behaviour, and $b = 0.5$ signifying a shift to a diffusion-controlled process governed by semi-infinite diffusion.[53] Fig. 6(d) reveals that the CNMS3 electrode exhibits a linear i–ν relationship, with calculated b-values of 0.48 (oxidation) and 0.51 (reduction), indicating a pseudocapacitive behaviour dominated by diffusion-controlled processes. To elucidate the contribution of capacitance and diffusion control at various scan rates, Trasatti equation was used as represented below.[54]

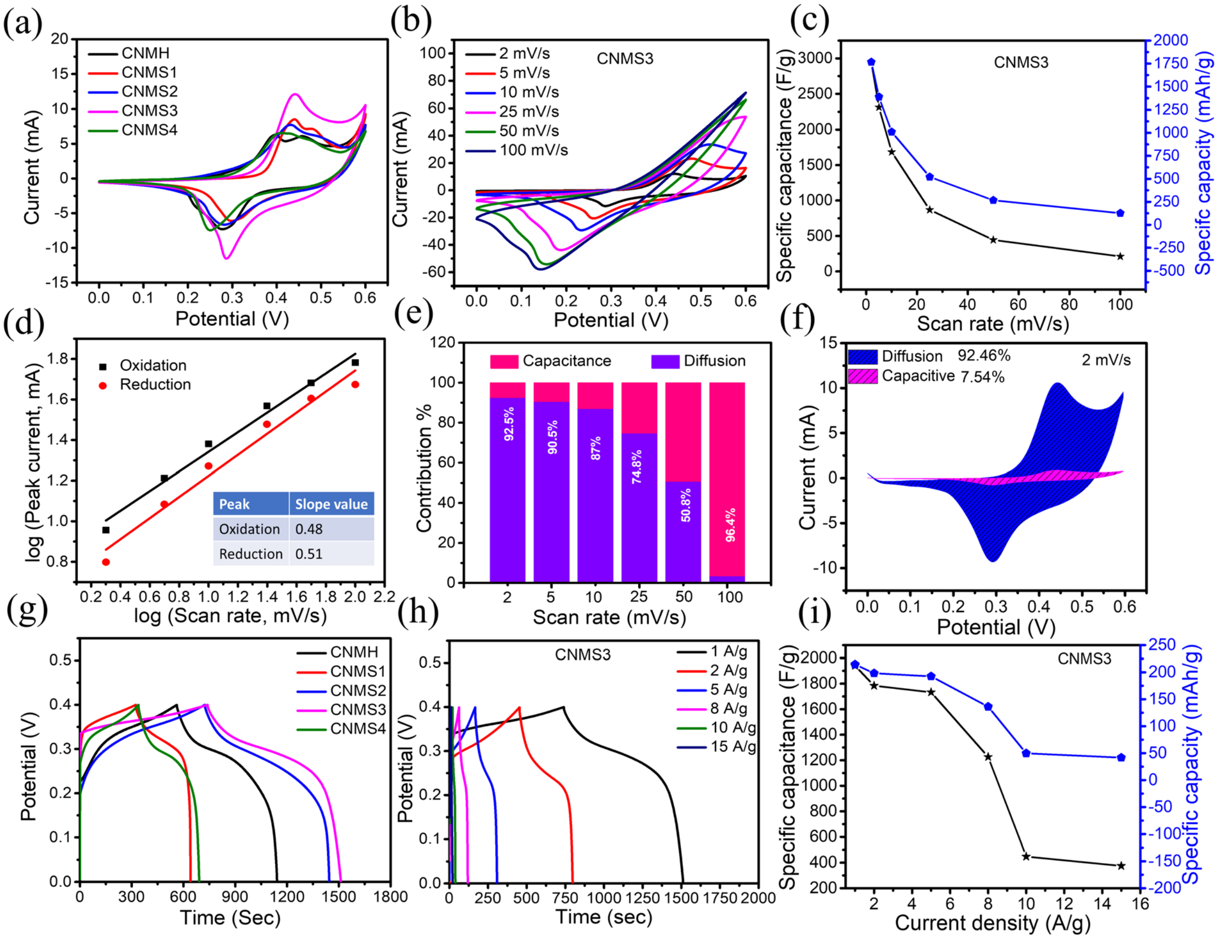

Fig. 6 (a) CV of all the electrodes at a scan rate of 2 mV s^{-1}, (b) CV of CNMS3@NF at different scan rates, (c) variation of specific capacitance with scan rates in CNMS3, (d) relationship between log *i* *vs.* log *V*, (e) comparision of diffusion and capacitance contribution percentage at different scan rates of CNMS3@NF, (f) determination of capacitance contribution of CNMS3@NF from CV data at 2 mV s^{-1}, (g) GCD graphs of all the electrodes at 1 A g^{-1}, (h) GCD plot of CNMS3@NF at various current densities from 1–15 A g^{-1}, (i) variation of specific capacitance with current densities in CNMS3.

$$i(v) = k_1 v + k_2 v^{1/2} \tag{8}$$

Which suggests that the current response (i) at a specific potential (V) consists of two distinct contributions: a surface-related capacitance-controlled component ($k_1 v$) and a diffusion-controlled component ($k_2 v^{1/2}$), which together govern the overall electrochemical behavior. Following to this explanation the capacitance and diffusion contribution in CNMS3 electrode has been illustrated in Fig. 6(e). The analysis reveals a significant decrease in diffusion-controlled processes with increasing scan rates, attributed to the restricted ion diffusion into the bulk material at higher scan rates. At a scan rate of 100 mV s^{-1}, capacitance-controlled processes predominate, reaching a dominant contribution of 96.4%. Meanwhile, Fig. 6(f), displays the capacitive contribution is plotted against various potential at a particular scan rate.[57] Notably, the CNMS3 electrode exhibits a capacitive contribution of approximately 7.5%, indicating that the diffusive mechanism is the predominant factor influencing the overall capacitance at a scan rate of 2 mV s^{-1}. To further assess the capacitive behavior, Galvanostatic Charge–Discharge (GCD) tests were conducted on all samples at a current density of 1 A g^{-1} (Fig. 6(g)). Consistent with the CV results, the GCD curves of CNMS3 exhibited the longest discharge time, featuring a distinct plateau. The observed specific capacitance values from the GCD curves are 1444 F g^{-1}, 798.7 F g^{-1}, 1800 F g^{-1}, 1940 F g^{-1}, and 877.7 F g^{-1} for CNMH, CNMS1, CNMS2, CNMS3 and CNMS4 electrode respectively at 1 A g^{-1}. This reveals that CNMS3 possesses outstanding capacitance and enhanced energy storage capabilities.[58] A comparison table of recent reported electrodes in literature along with this report has been represented in table1 below. Fig. 6(h) presents the GCD curve of the CNMS3 electrode at various current densities (1–15 A g^{-1}). This evidences that the GCD plot retains its shape with minimal change as the current density increases, demonstrating exceptional redox reversibility.[59] Additionally, the absence of a significant IR drop across all discharge regions suggests that the electroactive material is fully utilized in the redox reaction, highlighting the remarkable electronic conductivity of the electrode.[60] The GCD profiles of other compared electrodes are also presented with different

Table 1 Comparision table of our work with recent reported literatures

Sl no.	Electrode	Synthesis route	Electrolyte	Specific capacitance	Current density	Energy density	Power density	References
1	NiCoMoS@CC	One-step electrodeposition	2 M KOH	10 860.0 mF cm^{-2}	1 mA cm^{-2}	0.600 mW h cm^{-2}	0.800 mW cm^{-2}	28
2	NiCoMo-LDH@NiCoMoS	Hydrothermal	2 M KOH	7.73 F cm^{-2}	10 mA cm^{-2}	0.25 mW h cm^{-2}	40 mW cm^{-2}	55
3	NiCoMo@CC	Hydrothermal	2 M KOH	8.84 F cm^{-2}	8 mA cm^{-2}	0.64 mW h cm^{-2}	3.2 mW cm^{-2}	44
4	$Ni_2Co_2Mo_4S$@CC	Microwave hydrothermal	6 M KOH	177.2 mA h g^{-1}	1 A g^{-1}	39.2 Wh kg^{-1}	783 W kg^{-1}	8
5	Mo–Co–Ni–S	Electrodeposition	1 M KOH	2.39 F cm^{-2}	5 mA cm^{-2}	—	—	56
6	NiCoMoS@$Mo_{0.75}$-LDH	Hydrothermal	3 M KOH	1158 C g^{-1}	1 A g^{-1}	60.98 Wh kg^{-1}	2700 W kg^{-1}	34
7	$NiCoMoS_2$/1@NiCoAl-LDH	Hydrothermal	3 M KOH	1336.0 C g^{-1}	1 A g^{-1}	41.9Wh kg^{-1}	800 W kg^{-1}	45
8	CNMS@NF	Hydro/solvothermal	3 M KOH	1940 Fg^{-1} (215.5 mAh g^{-1})	1 A g^{-1}	349.2 Wh kg^{-1}	1631 Wk g^{-1}	This work

current densities in Fig. S9. Fig. 6(i) represents variation of specific capacitance and specific capacity of CNMS3 electrode at varying current densities. As the current density increases from 1 to 15 A g^{-1}, the specific capacitance of the CNMS3 electrode exhibits a gradual decline. The calculated specific capacitance (specific capacity) values of CNMS3 were 1940 F g^{-1} (215.5 mAh g^{-1}), 1784 F g^{-1} (198.2 mAh g^{-1}), 1732.5 F g^{-1} (192.5 mAh g^{-1}), 1226 F g^{-1} (136.2 mAh g^{-1}), 447.5 F g^{-1} (49.7 mAh g^{-1}), and 375 F g^{-1} (41.6 mAh g^{-1}) at current densities of 1, 2, 5, 8, 10, and 15 A g^{-1}, respectively (Fig. 6(i)). This decrease can be attributed to the reduced utilization of electroactive sites at higher scanning rates. However, CNMS3 retains a remarkable specific capacitance of approximately 375 F g^{-1} at 15 A g^{-1}, demonstrating a rate performance of around 19.3%. The energy storage properties of the optimized electrode CNMS3@NF were assessed, resulting in a high energy density of 349.2 Wh kg^{-1} and a power density of 1631 W kg^{-1}.

Electrochemical Impedance Spectroscopy (EIS) provides vital insights into the resistive and capacitive behaviour of electrode materials. As illustrated in Fig. 7(a), the intercept at the high-frequency region of the Nyquist plot corresponds to the equivalent series resistance (R_s), which includes contributions from the intrinsic resistance of the electrode, the electrolyte, and the contact interface. The measured R_s values for CNMH, CNMS1, CNMS2, CNMS3, and CNMS4 are 4.2, 2.9, 2.3, 2.1, and 8.2 Ω, respectively. Among them, CNMS3 exhibits the lowest R_s, indicating superior electrical conductivity and better electrode–electrolyte contact. The semicircle observed in the mid-frequency region of the Nyquist plot reflects the charge transfer resistance (R_{ct}), which is indicative of the interfacial kinetics between the electrolyte ions and active material. The smaller semicircle radius in CNMS3 suggests a lower R_{ct}, confirming more efficient charge transfer processes. Additionally, the steeper slope in the low-frequency region indicates lower diffusion resistance, attributed to the porous, hierarchically structured nanoflower morphology formed through optimized sulfidation. This architecture facilitates rapid ion transport and increases the accessibility of electroactive sites, thereby enhancing the faradaic redox processes. Further insight into the interfacial response dynamics is provided by the Bode phase angle plot (Fig. 7(b). The relaxation time (τ_0), which quantifies the minimum time required for efficient ion exchange at the electrode–electrolyte interface, was calculated using the relation $\tau_0 = 1/f_0$, where f_0 is the characteristic frequency at a phase angle of 45°.[61] Among all samples, CNMS3 displays the shortest τ_0, suggesting faster interfacial kinetics and superior charge transport behaviour. The τ_0 values of all electrodes are summarized in Table 2, reinforcing the exceptional performance of CNMS3. The cycling stability of the CNMS3@NF electrode was assessed through continuous cyclic voltammetry (CV) for 4000 cycles at a scan rate of 100 mV s^{-1} (Fig. 7(c)). Impressively, the electrode retains 70% of its initial

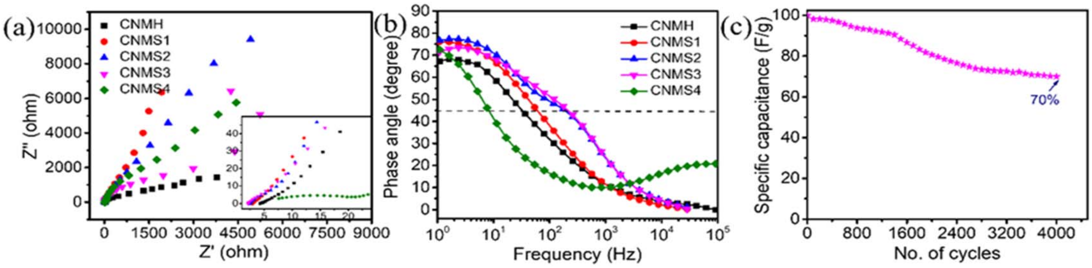

Fig. 7 Nyquist profiles, (b) Bode plot of all electrodes, (c) cyclic stability of CNMS3@NF at 100 mV s^{-1}.

Table 2 Tabulated values of f_0, τ_0 and R_s

Sample	f_0 (Hz)	τ_0 (sec)	R_s (ohm)
CNMH	32	0.031	4.2
CNMS1	59.28	0.016	2.9
CNMS2	173.1	0.005	2.3
CNMS3	218.51	0.004	2.1
CNMS4	8.25	0.121	7.5

capacitance, underscoring its excellent structural robustness and electrochemical durability over prolonged operation. This decay after ~1500 CV cycles is mainly attributed to structural and interfacial instability of the sulfide framework under repeated redox cycling. Continuous ion insertion/extraction induces mechanical strain and volume variation, which may generate microcracks and partial detachment of the nanostructure, reducing active surface area and breaking electronic pathways. The retained performance is attributed to the synergistic effect of multi-metal sulfides, structural integrity of the nanoflower morphology, and enriched S^{2-} species that mitigate active material degradation. To further examine the structural stability and morphological retention, XRD and SEM analyses of the CNMS3 electrode were carried out after the stability test. The post-stability XRD analysis reveals a decrease in crystallinity, but the phase remains unchanged after long-term cycling, confirming the material's structural stability (Fig. S10).[62]

The post-cycling morphologies of CNMS3@NF are shown in the Fig. S11. The images suggest that, while the nanoflower structure is generally maintained, surface roughening and partial detachment from the nickel foam have taken place, likely leading to the observed decrease in cycling performance. The EIS measurement of CNMS3 electrode was performed at intervals of 200 cycles, during the cycle tests which is illustrated in Fig. S12. The plots show that the semicircle diameter in the high-frequency region increases after cycling, indicating an increase in R_{ct} and R_s due to partial surface degradation and loss of active sites. In the low-frequency region, the slope becomes less vertical, reflecting slower ion diffusion at the electrode–electrolyte interface. These observations suggest that repeated cycling induces structural stress, microcracks, and partial dissolution of the active material, which collectively reduce the electrode's conductivity and electrochemical reversibility. Furthermore, as the number of cycles increases, the overall resistance rises, contributing to the observed decrease in conductivity.

The ICP-OES analysis was conducted to determine the metal composition of CNMS3@NF before and after the stability test. The results reveal a significant change in the metal composition compared to the pristine state. Before the stability test, the atomic percentage of metals in CNMS3@NF was 6.94% Ni, 28.54% Mo, and 25.52% Co. However, after the stability test, the ICP-OES analysis showed that the atomic percentage of metals had changed to 0% Ni, 6.92% Mo, and 16.58% Co as represented in table S1 in SI. These results suggest that the electrochemical process led to the leaching of Ni and some amount of Co along with Mo from the electrode surface, resulting in a change in the material's composition.

Conclusions

In summary, ternary CoNiMo sulfide (CNMS3@NF) nanostructured flowers were efficiently fabricated on NF using combined solvothermal and controlled sulfidation process. The effect of sulfur concentration on the nanostructures and electrochemical properties of CNMS was systematically investigated. It has been analyzed that the optimized S concentration on CNMH enhanced the specific capacitance value by more than 34%. It revealed that a sulfur concentration of 0.025 mM was found to significantly enhance the electrical conductivity of CNMS3@NF, yielding optimal electrochemical performance. The CNMS3 sample demonstrates exceptional specific capacitance of 1940 F g^{-1} at 1 A g^{-1}, along with outstanding rate capability, retaining 70% of its capacitance at 100 mV s^{-1}. To further improve the cycling stability of CNMS3@NF, future work could focus on optimizing the nanoflower architecture to alleviate structural stress during repeated redox cycles, applying protective coatings or conductive carbon matrices to prevent active material dissolution, and tailoring the electrolyte to suppress side reactions and material detachment. These strategies are expected to enhance long-term stability while preserving high specific capacity. Moreover, it exhibits a remarkable energy density of 349.2 Wh kg^{-1} at a power density of 1631 W kg^{-1}. This research provides a facile, efficient, and cost-effective strategy for synthesizing transition metal sulfides on NF, serving as a binder-free electrode, and paving the way for the development of next-generation high-performance supercapacitors.

Conflicts of interest

The Authors declare no competing financial interest.

Data availability

All data supporting the findings of this study are available within the article and its supplementary information (SI). Additional raw data can be obtained from the corresponding author upon reasonable request. Supplementary information: GCD and CV for CNMH and CNMS3 at different conditions; XPS survey spectra for CNMH and CNMS3; TEM and SAED for CNMH and CNMS3 at different resolutions; EDS mapping for CNMH; CV plot for CNMH, CNMS1, CNMS2, CNMS4 at various scan rates; specific capacitance *vs.* scan rate CNMH, CNMS1, CNMS2, CNMS4. GCD plot for CNMH, CNMS1, CNMS2, CNMS4. XRD, SEM, EIS, ICP for CNMS3 after stability test. See DOI: https://doi.org/10.1039/d5se01081k.

Acknowledgements

T. T. M. acknowledges C. V. Raman Global University, Bhubaneswar, Odisha, India, for the doctoral fellowship. T. T. M. and D. R. thank Prof. Satyajit Hazra and Mr Gautam Sarkar, Saha

Institute of Nuclear Physics, for providing XPS characterization facilities. Additionally, M. C. acknowledges the Council of Scientific and Industrial Research, Human Resource Development Centre (CSIR-HRDG) for the financial support with project No. 03WS (001)/2023-24/EMR-II/ASPIRE. J. N. B. thanks the Department of Atomic Energy (DAE), Govt. of India, for the research grant to NISER (RIN 4002-Basic Research in Chemical Sciences) and SERB, DST, for the award of a research grant CRG/2021/006499 to JNB.

References

1 L. Xia, K. Li, Y. Zhang, H. Wu, Z. Fang, X. Yan, B. Sa, L. Wang, L. Lin, J. Lin, G. Wei, D.-L. Peng and Q. Xie, *J. Mater. Chem. A*, 2024, **12**, 17222–17228.

2 X. Jian, H. Li, H. Li, Y. Li and Y. Shang, *Carbon*, 2021, **172**, 132–137.

3 K. K. Jaiswal, C. R. Chowdhury, D. Yadav, R. Verma, S. Dutta, K. S. Jaiswal, B. Sangmesh and K. S. K. Karuppasamy, *Energy Nexus*, 2022, **7**, 100118.

4 S. V. Sadavar, S.-Y. Lee and S.-J. Park, *Adv. Sci.*, 2024, **11**, 2403172.

5 A. G. Olabi, Q. Abbas, A. Al Makky and M. A. Abdelkareem, *Energy*, 2022, **248**, 123617.

6 J. Zhang, J. Luo, Z. Guo, Z. Liu, C. Duan, S. Dou, Q. Yuan, P. Liu, K. Ji, C. Zeng, J. Xu, W.-D. Liu, Y. Chen and W. Hu, *Adv. Energy Materials*, 2023, **13**, 2203061.

7 X. Li, G. Wang, X. Wang, X. Li and J. Ji, *J. Mater. Chem. A*, 2013, **1**, 10103–10106.

8 B. Chen, S. Peng, X. Wang, L. Dai, Y. Wu, Q. Xie and Y. Ruan, *ACS Appl. Nano Mater.*, 2024, **7**, 9658–9667.

9 M. A. Dar, S. R. Majid, M. Satgunam, C. Siva, S. Ansari, P. Arularasan and S. Rafi Ahamed, *Int. J. Hydrogen Energy*, 2024, **70**, 10–28.

10 M. Chakraborty, A. Biswal, D. P. Beura, D. Mohanty, T. T. Mishra, S. Mishra, D. Roy and J. N. Behera, *Energy Fuels*, 2025, **39**, 16715–16736.

11 M. Li, A. Addad, M. Dolci, P. Roussel, Mu. Naushad, S. Szunerits and R. Boukherroub, *Chem. Eng. J.*, 2020, **396**, 125370.

12 C. Chen, Q. Liang, Y. Mo, X. Zhang, X. Luo, J. Wu, P. Hu and Y. Chen, *Energy Technol.*, 2021, **9**, 2100297.

13 F. Ahmad, M. Zahid, H. Jamil, M. A. Khan, S. Atiq, M. Bibi, K. Shahbaz, M. Adnan, M. Danish, F. Rasheed, H. Tahseen, M. J. Shabbir, M. Bilal and A. Samreen, *J. Energy Storage*, 2023, **72**, 108731.

14 A. C. Mendhe, S. Dhas, Y. Kim and D. Kim, *Chem.–Eng. J.*, 2024, **496**, 153857.

15 A. Mamani, D. Barreda, M. Fabiana Sardella, M. Bavio, C. Blanco, Z. González and R. Santamaría, *Electroanal. Chem.*, 2024, **965**, 118366.

16 T. T. Mishra, C. K. Parashar, P. S. G. Pattader, F. Mayanglambam, M. Chakraborty and D. Roy, *Chemnanomat*, 2025, **11**(5), e202400635.

17 S. S. Singha, S. Rudra, S. Mondal, M. Pradhan, A. K. Nayak, B. Satpati, P. Pal, K. Das and A. Singha, *Electrochim. Acta*, 2020, **338**, 135815.

18 G. Tang, W. Tang, Q. Li, B. Tian, X. Zhang, J. Liang and W. Wu, *Small*, 2024, **20**, 2402609.

19 T. T. Mishra, M. Chakraborty, C. K. Parashar, J. Mahanta, P. S. G. Pattader and D. Roy, *J. Mater. Sci.: Mater. Electron.*, 2025, **36**, 180.

20 S. Rui, Z. Li, L. Meng, Q. Wang, J. Xu, Y. Zhao, Q. Jia, H. Li, S. Lu and Y. Zhang, *J. Mater. Chem. C*, 2025, **13**, 849–857.

21 A. Padhy, S. Lakshmy, B. Chakraborty and J. N. Behera, *Sustain. Energy Fuels*, 2023, **7**, 5271–5282.

22 R. K. Tripathy, A. Padhy, N. Sahu and J. N. Behera, *Sustain. Energy Fuels*, 2022, **6**, 4146–4152.

23 A. Padhy, R. Samal, C. S. Rout and J. N. Behera, *Sustain. Energy Fuels*, 2022, **6**, 2010–2019.

24 M. K. Sahoo, P. Mane, B. Chakraborty and J. N. Behera, *Inorg. Chem.*, 2024, **63**, 6383–6395.

25 D. Chu, X. Zhao, B. Xiao, A. Libanori, Y. Zhou, L. Tan, H. Ma, H. Pang, X. Wang, Y. Jiang and J. Chen, *Chem.–Eur. J.*, 2021, **27**, 8337–8343.

26 Z. Huang, W. Zhou, M. Hu, M. Zhang, X. Zhao, Y. Li, X. Hao, D. Li and J. Xu, *Chem. Eng. J.*, 2024, **494**, 152907.

27 W. Yan, H.-Y. Zeng, K. Zhang, Y.-W. Long and M.-X. Wang, *J. Colloid Interface Sci.*, 2023, **635**, 379–390.

28 D. Li, Y. Li, Y. Chen, Y. Dong, J. Hu, J. Zhao, S. Zhao, Y. Fu, D. He and J. Li, *J. Energy Storage*, 2024, **102**, 114253.

29 Y. Ye, X. Guo, Y. Ma, Q. Zhao, Y. Sui, J. Song, W. Ma, P. Zhang and C. Qin, *J. Electroanal. Chem.*, 2021, **897**, 115588.

30 A. Pramanik, S. Sengupta, S. K. Saju, S. Chattopadhyay, M. Kundu and P. M. Ajayan, *Adv. Energy Materials*, 2024, **14**, 2401657.

31 D. Luo, J. Zou, B. Ma, Z. Wei, X. Ye, Y. Wu, L. Zhang, Q. Wang and L.-A. Ma, *J. Alloys Compd.*, 2024, **1004**, 175798.

32 J. Zou, D. Luo, W. Li, H. Chen, Z. Wei, X. Ye, X. Wen and L.-A. Ma, *J. Power Sources*, 2025, **646**, 237260.

33 M. Yang, X. Wang, Y. Chen, Y. Du, S. Zou, A. Emin, X. Song, Y. Fu, Y. Li, J. Li and D. He, *Electrochim. Acta*, 2021, **398**, 139324.

34 Y. Sun, X. Wang and X. Wu, *Mater. Res. Bull.*, 2023, **158**, 112073.

35 M. Z. Iqbal, U. Aziz, S. Aftab, A. A. Ifseisi and M. Z. Ansari, *Mater. Chem. Phys.*, 2023, **309**, 128384.

36 G. T. Chavan, R. U. Amate, H. Lee, A. Syed, A. H. Bahkali, A. M. Elgorban and C.-W. Jeon, *J. Energy Storage*, 2023, **61**, 106757.

37 H. Reddy Inta, H. V. S. R. M. Koppisetti, S. Ghosh, A. Roy and V. Mahalingam, *ChemElectroChem*, 2023, **10**, e202201041.

38 S. Yasnur, S. Saha, A. Ray, M. Das, A. Mukherjee and S. Das, *ChemSelect*, 2021, **6**, 9823–9832.

39 T. T. Mishra, M. Chakraborty, J. N. Behera and D. Roy, *Energy Fuels*, 2024, **38**, 9186–9217.

40 U. Hamayun, M. A. Marwat, S. M. Abdullah, R. Ullah, M. Humayun, M. Bououdina, M. R. A. Karim, M. Z. Khan and M. B. Hanif, *J. Alloys Compd.*, 2025, **1012**, 178422.

41 J. Fan, Z. Meng, A. Chen, Z. Zhang, Y. He, H. Gao, H. Han, C. Liang and Y. Liu, *Mater. Sci. Semicond. Process.*, 2025, **188**, 109223.

42 Y. B. Chen, J. J. You, Y. H. Chen, L. A. Ma, H. X. Chen, Z. H. Wei, X. Y. Ye and L. Zhang, *CrystEngComm*, 2022, **24**, 5238–5250.

43 X. Yang, Z. Dong and C. Q. Sun, *Appl. Phys. Lett.*, 2024, **9**, e202303817.

44 D. Luo, Y. Chen, J. Zou, Z. Wei, L. Zhang, X. Ye, Q. Wang and L.-A. Ma, *J. Energy Storage*, 2023, **74**, 109322.

45 K. Zhang, H.-Y. Zeng, M.-X. Wang, H.-B. Li, W. Yan, H.-B. Wang and Z.-H. Tang, *J. Mater. Chem. A*, 2022, **10**, 11213–11224.

46 C. Zhang, Q. Sui, L. Lu, Y. Zou, F. Xu, L. Sun, D. Cai and C. Xiang, *J. Energy Storage*, 2023, **61**, 106691.

47 Y. Wei, Y. Lv, B. Guo and J. Gong, *J. Energy Chem.*, 2021, **57**, 587–592.

48 P. Li, C. Ruan, J. Xu and Y. Xie, *Electrochim. Acta*, 2020, **330**, 135334.

49 M. Gao, K. Le, D. Xu, Z. Wang, F. Wang, W. Liu, H. Yu, J. Liu and C. Chen, *J. Alloys Compd.*, 2019, **804**, 27–34.

50 Y. Lu, J. Liang, S. Deng, Q. He, S. Deng, Y. Hu and D. Wang, *Nano Energy*, 2019, **65**, 103993.

51 J. Kang, A. Hirata, L. Chen, S. Zhu, T. Fujita and M. Chen, *Angew. Chem.*, 2015, **127**, 8218–8222.

52 L. Lv, Z. Li, K.-H. Xue, Y. Ruan, X. Ao, H. Wan, X. Miao, B. Zhang, J. Jiang, C. Wang and K. (Ken) Ostrikov, *Nano Energy*, 2018, **47**, 275–284.

53 R. Velayutham, R. Manikandan, C. Justin Raj, A. Dennyson Savariraj, W.-J. Cho, H.-M. Jang and B. Chul Kim, *Appl. Surf. Sci.*, 2021, **570**, 151051.

54 H. Liu, D. Zhao, P. Hu, K. Chen, X. Wu and D. Xue, *Mater. Today Phys.*, 2020, **13**, 100197.

55 D. Luo, J. Zou, Z. Wei, X. Ye, Q. Wang and L.-A. Ma, *CrystEngComm*, 2023, **25**, 6361–6370.

56 M. Lv, X. Zhang, F. Wang, T. Yu, H. Lv, Y. Zhai, Y. Shen and G. Lv, *Nanotechnology*, 2020, **31**, 225603.

57 C. Costentin, *J. Phys. Chem. Lett.*, 2020, **11**, 9846–9849.

58 S. Khalid, Y. Khan, E. Ahmed, S. Nawaz, N. R. Khalid and W. Ahmed, *Emerging Nanotechnol. Renewable Energy*, ed. W. Ahmed, M. Booth and E. Nourafkan, Elsevier, 2021, pp. 407–445.

59 Y. Tang, H. Shen, J. Cheng, Z. Liang, C. Qu, H. Tabassum and R. Zou, *Adv. Funct. Mater.*, 2020, **30**, 1908223.

60 H. Chevulamaddi and V. R. Kalagadda, *Mater. Today Sustain.*, 2025, **29**, 101054.

61 L. Zhao, H. Guo, Y. Li, Z. Liu and R. Song, *Nanoscale*, 2024, **16**, 1880–1889.

62 A. Sahu, M. Sadangi and J. N. Behera, *Sustain. Energy Fuels*, 2025, **9**, 2718–2728.